

A cobalt-organic framework with sensitive detection of Fe^{3+} , $\text{Cr}_2\text{O}_7^{2-}$, and CrO_4^{2-} ions in water

Zhen Zhang

Yunnan University

Han-Xu Sun

Yunnan University

Shi-Fen Li

Yunnan University

Rui-Dong Wang

Yunnan University

Lin Du

Yunnan University

Ming-Jin Xie

Yunnan University

Jie Zhou

Yunnan University

Qi-Hua Zhao (✉ qhzhao@ynu.edu.cn)

Yunnan University

Original Research Full Papers

Keywords: Metal-organic framework, cds topology, Fluorescence, Sensing, Hirshfeld surface analysis

Posted Date: February 8th, 2021

DOI: <https://doi.org/10.21203/rs.3.rs-161017/v1>

License:  This work is licensed under a Creative Commons Attribution 4.0 International License.

[Read Full License](#)

Version of Record: A version of this preprint was published at Journal of Inorganic and Organometallic Polymers and Materials on February 25th, 2021. See the published version at <https://doi.org/10.1007/s10904-021-01917-2>.

Abstract

A six-coordinated 3D metal–organic framework (MOF), namely, $[\text{Co}(\text{BPDC})(3\text{-bpdb})(\text{H}_2\text{O})_2]_n$ (**1**) (H_2BPDC = 4,4'-biphenyldicarboxylic acid, 3-bpdb = 1,4-bis(3-pyridyl)-2,3-diaza-1,3-butadiene) was purposefully constructed and characterized by single-crystal XRD, IR, elemental analyses, PXRD, SEM, and TGA. Crystal structural analysis revealed that the complex consists of a **cds**-type three-fold interpenetrated framework. Hirshfeld surface analysis yielded details of the surface characteristics of **1**. Significant O–H \cdots O hydrogen bonding interactions, which could promote the stability of the framework, were found. **1** is extremely stable in aqueous solution and can resist acids and bases over an extensive pH range of 2–13. **1** shows brilliant fluorescent emission in the solid state and in aqueous solution. Fluorescence titration, cyclic, and anti-interference experiments demonstrated that **1** is an excellent probe for Fe^{3+} , CrO_4^{2-} and $\text{Cr}_2\text{O}_7^{2-}$ in water. The K_{sv} values of **1** for Fe^{3+} , CrO_4^{2-} , and $\text{Cr}_2\text{O}_7^{2-}$, which were as high as $1.06 \times 10^4 \text{ M}^{-1}$, $1.50 \times 10^4 \text{ M}^{-1}$, and $1.16 \times 10^4 \text{ M}^{-1}$, respectively, were comparable with those of other sensors. The quenching mechanism of the novel probe was subsequently explained.

1. Introduction

Recent developments in society and significant improvements in living standards have brought increased attention to the state of the environment and its relation to human health. Following the establishment of modern industries, heavy metal ion pollution and toxic inorganic anion contamination from industrial effluents slowly became among the greatest environmental threats to humans and the ecological environment. [1–4]. Fe(III), a trivalent metal ion considered essential for all organisms, plays a vital role in a number of crucial processes. A shortage or excess of this metal in the body results in serious functional disorders [5, 6]. Cr(VI) ions serve as important oxidants in industrial production but can cause acute diseases even at very low concentrations [7]. As ion pollution caused by industrial development runs counter to the current pursuit of green environmental protection, solutions to this problem must be quickly developed. However, because of portability problems and the cost of transporting and maintaining sophisticated instruments in actual field use, the current detection methods for these ions are limited [8]. Researchers are actively developing new materials for wastewater treatment and pollution prevention. For example, nanostructure semiconductor-mediated photocatalysis can effectively degrade organic pollutants in water [9]. Inorganic metal oxide semiconductor-based photocatalysts play a key role in the photocatalytic treatment of water pollution [10], and photocatalytic nanostructured semiconducting thin films can be used for the photodegradation of toxic chemicals in the environment [11]. Polymer membrane pervaporation separation for alcohol dehydration is believed to be a suitable candidate technology to replace traditional distillation methods [12]. Developing a cost-effective and selective material that can effectively detect both Fe(III) and Cr(VI) is an urgent and important undertaking. Fluorescent probes can address the limitations of the available materials and achieve simple and fast detection.

Fluorescent metal–organic frameworks (MOFs) are excellent functional materials that have been synthesized in large quantities. These frameworks usually have fascinating structures with novel topologies and can be functionally modified. Over the last few years, significant progress has been made in the detection of metal ions using fluorescent MOF materials [13–16]. In general, the fluorescent MOFs are constructed with aromatic ligands because the π electron systems of the ligands endow the MOFs with photoluminescence properties and provide potential supramolecular recognition sites between the backbones and analytes [17]. The mixed-ligands approach is implemented by the judicious choice of carboxylates with aromatic π rings and N-donor linkers can afford novel fluorescent MOFs [18, 19]. Among the transition metal ions, Co^{2+} is widely used in the synthesis of MOFs because of its excellent coordination ability and potential function as an electrochemically active center; moreover, it is widely abundant and inexpensive. However, compared with other d^{10} electron configuration transition metal ions (e.g., Zn^{2+} , Cd^{2+}), Co^{2+} is rarely used in fluorescence MOF sensors [20–22].

Because of its large π -conjugated structure, 4,4'-biphenyldicarboxylic acid (H_2BPDC) is considered a good mixed ligand component. The molecule presents excellent flexibility through the free rotation of two benzene rings or carboxylate groups and phenyl rings, which eventually leads to structural diversity, as well as good coordination ability and stability under acidic and basic conditions [23–26]. As a neutral bis-pyridyl-based ligand, 4-bis(3-pyridyl)-2,3-diaza-1,3-butadiene (3-bpdb) has been reported to be an efficient bidentate bridging connector for the construction of coordination architectures [27–30]. The ligand not only possesses conformational freedom but also exhibits the nonbonded functional sites of the diaza group, which could interact with metal ions. Given the aforementioned considerations, Co^{2+} was assembled with the π -conjugated organic molecules H_2BPDC and 3-bpdb to obtain a 3D luminescent Co-MOF, $[\text{Co}(\text{BPDC})(3\text{-bpdb})(\text{H}_2\text{O})_2]_n$ (**1**), which was then structurally characterized. The excellent fluorescent characteristics of **1** demonstrate its potential use as a potential fluorescent probe for detecting Fe^{3+} , CrO_4^{2-} , and $\text{Cr}_2\text{O}_7^{2-}$.

2. Experimental Section

2.1. Materials and methods

3-bpdb was prepared according to the reported literature [31]. H_2BPDC were obtained from Adamas company, purity 98%+, grade RG. $\text{Co}(\text{NO}_3)_2 \cdot 6\text{H}_2\text{O}$ were obtained from Beijing Yinuokai Technology Co., Ltd., purity 99%, grade RG. All other analytical-grade chemicals and solvents were commercially available and used as received without further purification. Elemental analyses for C, H, and N were carried out with an Elementar Vario ELIII analyzer. The IR absorption spectra of all the complexes were collected using KBr pellets on a Thermo Scientific FTIR-Nicolet iS10 spectrometer in the range $4000\text{--}400\text{ cm}^{-1}$. PXRD patterns of these compounds were recorded on a Rigaku X-ray diffractometer with $\text{Cu-K}\alpha$ radiation ($\lambda = 1.5418\text{ \AA}$). Simulation of the PXRD patterns were performed using single-crystal data and processed with the Mercury 3.7 program available free of charge through the Internet at <http://www.iucr.org>.

Luminescence spectroscopy of all the compounds was performed on a Lengguang (Shanghai, China) F98 fluorescence spectrophotometer, and polarization-dependent photoluminescence studies were performed on a Hitachi F-7000 fluorescence spectrophotometer. The UV-Vis spectra were obtained using UV-240 IPC spectrophotometer. TGA data were acquired using a Mettler-Toledo simultaneous thermal analyzer from room temperature to 800 °C under an N₂ atmosphere with a heating rate of 10 °C min⁻¹. Molecular Hirshfeld surface calculations were performed using the CrystalExplorer 17.5 program [32]. Scanning electron microscopic (SEM) investigations were carried out using an FEI QUNTA field emission gun 650; prior to the SEM examination the specimens were sputter coated with gold. Variable-temperature susceptibility measurements of crystalline samples were performed on a Quantum Design MPMS-XL SQUID magnetometer. Diamagnetic corrections were performed from Pascal's constants, and an experimental correction for a sample holder was also applied. Point symbol and topological analyses were conducted by using the TOPOS program package [33].

2.2. Synthesis of complex 1

A mixture of 3-bpdb (20.1 mg, 0.1 mmol), Co(NO₃)₂·6H₂O (14.6 mg, 0.05 mmol), H₂BPDC (24.2 mg, 0.1 mmol), and DMF/H₂O (5 mL; 3:2, v:v) was placed in a 25 mL Teflon-lined stainless steel vessel, heated to 110 °C for 2 days, and then cooled to room temperature over 10 h. Pink block-shaped crystals suitable for XRD analysis were separated by filtration with the yield of 16.9 mg, 62% (based on Coll). Elemental analysis (%): calcd for (C₂₆H₂₂N₄CoO₆): C 57.26, H 4.06, N 10.27; Found: C 57.20, H 4.01, N 10.33. IR (KBr, cm⁻¹): 3440 (br), 1624 (m), 1577 (m), 1530 (m), 1423 (m), 1391 (s), 1312 (w), 774 (m), 696 (m), 678 (m), 431 (w).

2.3. Crystallographic

The selected single crystal with suitable dimensions was mounted on a glass fiber and used for X-ray diffraction analyses. Crystallographic data were collected at 293 K on a Bruker Smart APEX II CCD diffractometer with graphite-monochromated Mo-K α radiation ($\lambda = 0.71073 \text{ \AA}$) using ω -scan technique. Empirical absorption corrections were applied using the SADABS program [34]. The structure was solved in each case by using the SHELXL package and refined by the full matrix least-squares method based on F^2 using the SHELX-2014 program [35–38]. All of the non-hydrogen atoms were located in different Fourier syntheses and finally refined with anisotropic thermal parameters. Hydrogen atoms attached to the organic moieties were either located from the difference Fourier map or fixed stereochemically. Details of the crystallographic data collection and refinement parameters are summarized in Table 1, selected bond distances and angles are given in Table S1, hydrogen bonds are given in Table S2. The CCDC number of **1** was assigned to be 1953740.

Table 1
Crystallographic data for complex 1

Complex	1
Empirical formula	C ₂₆ H ₂₂ CoN ₄ O ₆
Formula weight	545.40
Temperature (K)	293(2)
Crystal system	Monoclinic
Space group	<i>C2/c</i>
<i>a</i> (Å)	26.118(4)
<i>b</i> (Å)	10.9943(18)
<i>c</i> (Å)	9.1219(15)
<i>α</i> (°)	90
<i>β</i> (°)	108.954(2)
<i>γ</i> (°)	90
Volume (Å ³)	2477.4(7)
<i>Z</i>	4
<i>D</i> _{calc} (g cm ⁻³)	1.462
Absorption coefficient (mm ⁻¹)	0.742
<i>F</i> (0 0 0)	1124
Limiting indices	-31 ≤ <i>h</i> ≤ 27
	-13 ≤ <i>k</i> ≤ 11
	-10 ≤ <i>l</i> ≤ 10
Data/restraints/parameters	2209 / 3 / 174
Goodness-of-fit on <i>F</i> ²	1.025
Final <i>R</i> indices [<i>I</i> > 2σ(<i>I</i>)]	<i>R</i> ₁ = 0.0373
	<i>wR</i> ₂ = 0.0894
<i>R</i> indices (all data)	<i>R</i> ₁ = 0.0572
	<i>wR</i> ₂ = 0.1030

Complex	1
Largest diff peak/hole (e Å ⁻³)	0.266, - 0.343

3. Results And Discussion

3.1. Crystal structure of complex 1

Single-crystal XRD analysis revealed that **1** is isostructural with our recently reported Ni-based MOF, [Ni(BPDC)(3-bpdb)(H₂O)₂]_n [30]. As illustrated in Fig. 1a, the structure of **1** consists of one Co(II) atom, one BPDC²⁻ anion, one 3-bpdb ligand, and two coordinated water molecules. Co1 is located on a crystallographic inversion center and shows a slightly distorted octahedral geometry (Scheme S1). The equatorial plane is built by two water-oxygen atoms and two carboxylate-oxygen atoms from two independent BPDC²⁻ ligands (Co1–O1 = 2.072(2) Å; Co1–O3 = 2.129(2) Å). Two nitrogen atoms from two 3-bpdb ligands occupy the axial positions, with the Co – N_{3-bpdb} bond length measuring 2.157(2) Å. These values are in agreement with those reported for Co(II) complexes [20–22]. The BPDC²⁻ anions in **1** display bis-single-dentate coordination modes and link Co(H₂O)₂ units to form 1D linear Co(H₂O)₂(BPDC) chains with Co···Co separations of 15.16 Å (Fig. 1b). As illustrated in Figs. 1c and d, these linear chains are bridged at Co(II) atoms by μ₂-3-bpdb spanning two different extending directions in an ABAB fashion to generate a 3D architecture. In **1**, the free torsions in BPDC²⁻ between two phenyl rings and between phenyl rings and carboxyl groups are 39.83(10)° and 3.87(1)°, respectively (Scheme S2).

Topologically, each six-coordinated Co(II) cation can be simplified as a 4-connect (4-c) node, and the ligands serve as linkers; thus, the whole structure of **1** can be represented as a uninodal, 4-c, **cds**-6^{5.8} net (Fig. 1e). The single **cds** net has a very large void, which is partially occupied by the two other nets to form a 3-fold interpenetrated framework (Fig. 1f). Significant O – H···O hydrogen bonds between H atoms from coordinated water molecules and the uncoordinated carboxylate O atoms of BPDC²⁻ are found in **1** (Fig. S1). These interactions stabilize the MOF molecules and strengthen the rigidity of the compound to a great extent, thereby promoting luminescence sensitivity [39]. **1** and [Ni(1,4-bdc)(3-bpdb)(H₂O)]_n exhibit the same 3D **cds** topology. The main difference between these two molecules is that the H₂BPDC ligand has a longer connection length than 1,4-benzenedicarboxylic acid (1,4-H₂bdc), which increases the degree of interpenetration from 2-fold in the above compound to 3-fold in **1**. Ligands with longer connection lengths were previously expected to yield MOFs with larger pores, but the pores generated were often occupied via the phenomenon of interpenetration.

3.2. Hirshfeld surface (HS) analysis

The Hirshfeld surface is a suitable tool for describing the surface characteristics of molecules [40]; it is used to analyze information about all existing weak/strong interactions in a crystal system, which is important in the crystal engineering point of view. The molecular Hirshfeld surfaces of **1** were generated

using a standard (high) surface resolution mapped with d_{norm} (Fig. 2) and d_i , d_e , *curvedness*, *shape index* (Fig. S2). In Fig. 2, the regions of 1A in bright red reflect hydroxyl oxygen O – H and carboxylate O (O–H···O–C) interactions, and the regions of 1B and 1C in red reflect metal coordination bonds with strong forces.

Significant intermolecular interactions mapped on the molecular surface can be clearly presented through 2D fingerprints. As shown in Figs. S3 and 4, 37.1% H···H interactions and 25.9% C···H/H···C interactions account for over half of the total number of interactions identified. The proportion of 15.7% represents typical O–H···O hydrogen bonds. The other hydrogen bonds of C–H···N may contain 8.7% N···H/H···N interactions. Reciprocal C···C contacts with 4.3% refer to weak π ··· π stacking, which is also important in the formation of the structure of **1**. These analytical results are highly consistent with the crystallographic structure of **1**.

3.3. PXRD, IR and Thermogravimetric analyses of **1**

The phase purity of the as-synthesized complex was confirmed by PXRD measurements. As shown in Fig. 3, the diffraction peaks of the bulk sample are consistent with the simulated pattern of the single-crystal data, which indicates that **1** mainly has one crystalline phase.

As shown in Fig. S5, the broad band of **1** in the 3300 – 3500 cm^{-1} region implies the existence of coordinated water molecules and hydrogen bonding interactions, consistent with the crystal structure of the sample. The absence of characteristic bands at approximately 1700 cm^{-1} indicates the complete deprotonation of carboxylate groups in H₂BPDC after reaction with the metal ions [41]. The vibrations of $\nu_{as}(\text{COO}^-)$ and $\nu_a(\text{COO}^-)$ are observed at 1577 and 1391 cm^{-1} , respectively. The absorption bands observed at about 430 cm^{-1} could be ascribed to metal–O stretching vibrations. These results are consistent with the crystal structure of **1**. Fig. S6 is the IR absorption spectra of **1** and 3-bpdb

The thermal stability of **1** was studied by TGA (Fig. S7). The TG curve of **1** indicates no obvious weight loss from ambient temperature to 172 °C, a weight loss of 6.32% from 172 °C to 225 °C, which is consistent with the loss of two coordinated water molecules (calcd: 6.61%), then the anhydrous compound successively decomposes.

3.4. Luminescence Behaviors

The solid-state fluorescence of the ligands and **1** was studied. The spectrum of H₂BPDC in Fig. 4a shows an emission band at 402 nm upon excitation at 346 nm, which can be ascribed to the ligand centered electronic transitions, that is, $\pi^* \rightarrow n$ or $\pi \rightarrow \pi^*$ transitions [42]. The spectrum of 3-bpdb shows a maximum emission peak at 394 nm and a shoulder peak at 469 nm ($\lambda_{ex} = 254$ nm, Fig. S8) [28]. **1** shows an emission peak at 397 nm ($\lambda_{ex} = 343$ nm), which is close to characteristic emission peak of the free H₂BPDC ligand. Since non-d¹⁰ metal-based coordination polymers are usually emission silent due to the d-d transition, the emission of **1** at 397 nm can be ascribed to the mixed contribution of intra-ligand and ligand-to-ligand charges [21–23]. To the best of our knowledge, fluorescent coordination compounds are

mainly based on Cd(II) and Zn(II) with a d^{10} electronic configuration; luminescent Co(II) MOFs are relatively rare. According to the literature [30], the isostructural compound $[\text{Ni}(\text{BPDC})(3\text{-bpdb})(\text{H}_2\text{O})_2]_n$ does not have similar luminescence properties.

The fluorescence properties of **1** in diverse solvent suspensions were investigated to explore its potential use as a probe for detecting ions. Finely ground samples of **1** were dispersed in different solvents, including H_2O , acetone, acetonitrile (CH_3CN), dimethyl acetamid (DMA), N,N-Dimethylformamide (DMF), dimethyl sulfoxide (DMSO), ethanol, iso-propanol, n-hexane, tetrahydrofuran (THF), and toluene, and then ultrasonicated for 30 min to form stable suspensions for the fluorescence studies. As shown in Fig. 4b, different solvents have different effects on the luminescence intensity of **1**, which can be attributed to solvent effects. The slight shift in the emission peak of **1** compared with its solid-state emission spectrum may be ascribed to interactions between the homogeneously dispersible framework and solvent molecules with different polarities [43].

3.5. Stability of **1** in acid-based solution

Stable existence in acidic/basic solutions is another important property of probes. **1** was immersed in acidic/basic solutions of pH 1–14 for 24 h, filtered and then subjected to PXRD. As shown in Fig. S9, the patterns of **1** before and after immersion treatment are consistent in the pH range of 2–13, which implies that the framework of **1** remains intact. These results demonstrate that **1** can exist stably in acidic/basic solutions.

3.6. Selective sensing of cations

Because **1** has good fluorescence properties and can resist acids and bases in aqueous solution, it may be used as a probe for detecting ions. Various aqueous solutions of $\text{M}(\text{NO}_3)_x$ (0.1 M) containing different metal ions ($\text{M}^{x+} = \text{Na}^+, \text{Mg}^{2+}, \text{Al}^{3+}, \text{K}^+, \text{Ca}^{2+}, \text{Cr}^{2+}, \text{Mn}^{2+}, \text{Co}^{2+}, \text{Ni}^{2+}, \text{Cu}^{2+}, \text{Zn}^{2+}, \text{Ag}^+, \text{Cd}^{2+}, \text{Pb}^{2+},$ and Fe^{3+}) were separately dropped into a suspension of **1**, which was obtained by dissolving **1** in aqueous solution and sonicating for 30 min to reach a stable state. The luminescence spectrum of the resulting solutions was obtained under same conditions. As shown in Figs. 5a and S10, only the solution containing Fe^{3+} display a significant quenching effect on the emission intensity of **1**, which indicates that **1** may be a potential fluorescent sensor for Fe^{3+} with high selectivity and sensitivity.

The sensitivity of **1** to Fe^{3+} ions was explored via quantitative fluorescence titration experiments. Fe^{3+} solution (50 mM) was gradually added dropwise to a suspension of **1**, after which the fluorescence intensity of the solution was measured at 393 nm. As shown in Fig. 5b, the emission intensity of **1** continuously decreases with increasing Fe^{3+} concentration. The quenching efficiency of Fe^{3+} ion pair **1** is as high as 92% when the concentration of Fe^{3+} is 0.79 mM (32 μL). The quenching efficiency of **1** was calculated by using the Stern-Volmer equation, $(I_0/I) = K_{sv}[A] + 1$. The SV plot for Fe^{3+} displays a very good linear relationship at low concentrations, and the K_{sv} value of the sensor toward Fe^{3+} is calculated as $1.06 \times 10^4 \text{ M}^{-1}$, which is comparable with that of other sensors for Fe^{3+} (Fig. S11) [16, 44, 45]

The recyclability of the probe determines whether it can be reused. Recovery experiments of **1** as an Fe^{3+} probe were carried out. Here, 50 mg of **1** was first immersed in Fe^{3+} solution (50 mM) to form $\text{Fe}^{3+}@1$. The sample was washed five times with distilled water to remove the Fe^{3+} , filtered, and then analyzed by PXRD. This procedure was repeated thrice. As shown in Fig. 6a, the fluorescence intensity of **1** was recovered compared with that of $\text{Fe}^{3+}@1$. PXRD also demonstrated that the framework of **1** remains intact after interacting with Fe^{3+} (Fig. 6b).

Because several ions often coexist in solution, the accurate detection of target metal ions under the interference of other metal ions must be ensured. Competitive experiments of $\text{Fe}^{3+}@1$ in the presence of other metal ions were performed. Fe^{3+} solution (1.6 mmol) was dropped into a suspension of **1** containing other metal ions (1.6 mmol). The fluorescence intensity of **1** was then detected and recorded, as shown in Fig. S12. The quenching effect caused by Fe^{3+} ions remains unchanged in the presence of other metal ions, thereby indicating that **1** can selectively identify Fe^{3+} against the interference of other analogs.

3.7. Selective sensing of anions

The versatility of **1** as a fluorescent probe for anions was investigated by adding various 0.1 M Na/K-anion aqueous solutions (i.e., Cl^- , Br^- , I^- , ClO_3^- , HPO_4^{2-} , H_2PO_4^- , CO_3^{2-} , SO_4^{2-} , and SCN^-) to an aqueous suspension of **1**. Interestingly, CrO_4^{2-} and $\text{Cr}_2\text{O}_7^{2-}$ demonstrate obvious quenching effects on the fluorescence of **1** (Figs. 7a and S13). The titration curves show that the fluorescence intensity of **1** decreased with increasing $\text{CrO}_4^{2-}/\text{Cr}_2\text{O}_7^{2-}$ concentration. The quenching efficiency between **1** and $\text{CrO}_4^{2-}/\text{Cr}_2\text{O}_7^{2-}$ is as high as 97% and 95% when the concentrations of $\text{CrO}_4^{2-}/\text{Cr}_2\text{O}_7^{2-}$ are 0.54 mM (22 μL) and 0.59 mM (24 μL), respectively (Figs. 7b and d). The K_{SV} values of **1** for CrO_4^{2-} and $\text{Cr}_2\text{O}_7^{2-}$, at 1.50×10^4 and $1.16 \times 10^4 \text{ M}^{-1}$, respectively, are comparable with those of other sensors reported as luminescent probes for these ions (Figs. 7c and e) [4, 16]. Recovery experiments of **1** as a $\text{CrO}_4^{2-}/\text{Cr}_2\text{O}_7^{2-}$ probe was carried out using the protocol adopted for the recovery experiments with Fe^{3+} . As shown in Fig. S14, the fluorescence intensity of **1** was recovered compared with those of $\text{CrO}_4^{2-}@1$ and $\text{Cr}_2\text{O}_7^{2-}@1$. PXRD demonstrated that the framework of **1** remains intact after regeneration. The anti-interference ability of **1** was measured through competitive experiments by the same method (Fig. S15). The quenching effect caused by $\text{CrO}_4^{2-}/\text{Cr}_2\text{O}_7^{2-}$ is fairly stable in the presence of other anions, thereby indicating that **1** can selectively recognize $\text{CrO}_4^{2-}/\text{Cr}_2\text{O}_7^{2-}$ and resist the interference of analogues.

3.8. Quenching mechanism

The quenching mechanism was investigated to understand the high selectivity and sensitivity of **1** toward Fe^{3+} and $\text{CrO}_4^{2-}/\text{Cr}_2\text{O}_7^{2-}$ better. The PXRD patterns of **1** were obtained after ion identification, and patterns identical to those of the as-synthesized materials were obtained. This result indicates that the skeleton of the samples is unchanged following ion detection. (Figs. 6b, S14b and S14d). **1** (20 mg)

was also immersed in 0.1 M $\text{Fe}(\text{NO}_3)_3$, K_2CrO_4 , and $\text{K}_2\text{Cr}_2\text{O}_7$ aqueous solutions for 2 days and then subjected to SEM analysis. The SEM micrographs obtained show no obvious changes in the surface of the material after treatment with different solutions compared with that of the blank sample. (Fig. S16). Hence, quenching is not caused by the destruction of the crystal framework. The quenching mechanism of **1** was explored by collecting the UV-Vis spectra of Fe^{3+} and $\text{CrO}_4^{2-}/\text{Cr}_2\text{O}_7^{2-}$ in water. (Fig. S17). The excitation spectrum (maximum emission peak, 346 nm) of **1** clearly overlaps with the absorption spectra of Fe^{3+} and $\text{CrO}_4^{2-}/\text{Cr}_2\text{O}_7^{2-}$. Thus, the luminescence quenching effect is due to competitive absorption between Fe^{3+} and $\text{CrO}_4^{2-}/\text{Cr}_2\text{O}_7^{2-}$ and **1**.

4. Conclusions

In summary, $[\text{Co}(\text{BPDC})(3\text{-bpdb})(\text{H}_2\text{O})_2]_n$ (**1**) was effectively synthesized under hydrothermal conditions and showed a 3-fold interpenetrated 3D structure and with a 4-c **cds**-type topology. The crystal displayed not only good thermal stability but also excellent stability in aqueous solution and could resist acids and bases over a wide pH range. Ion recognition experiments demonstrated that **1** can selectively identify Fe^{3+} and $\text{CrO}_4^{2+}/\text{Cr}_2\text{O}_7^{2+}$ with excellent regenerability and strong anti-interference ability. These results indicate that **1** is a promising candidate fluorescent sensing material for detecting Fe^{3+} , CrO_4^{2+} , and $\text{Cr}_2\text{O}_7^{2+}$.

Declarations

Acknowledgements

This work was supported by the National Natural Science Foundation of China (Project 21967019) and Yunnan Fundamental Research Projects (grant number 2016FB023).

Funding: This work was supported by the National Natural Science Foundation of China (Project 21967019) and Yunnan Fundamental Research Projects (grant number 2016FB023).

Conflicts of interest/Competing interests: No conflict of interest exists in the submission of this manuscript, and the manuscript is approved by all authors for publication. I would like to declare on behalf of my co-authors that the work described was original research that has not been published previously, and not under consideration for publication elsewhere, in whole or in part. All the authors listed have approved the manuscript that is enclosed.

Availability of data and material: CCDC 1953740 (1) contain the supplementary crystallographic data for this paper. The data can be obtained free of charge from the Cambridge Crystallographic Data Centre via http://www.ccdc.cam.ac.uk/data_request/cif.

References

1. P. A. Kobielska, A. J. Howarth, O. K. Farha, S. Nayak, *Coord. Chem. Rev.* **358**, 92 (2018)
2. T. O. Ajiboye, O. A. Oyewo, D. C. Onwudiwe, J. *Inorg. Organomet. Polym. Mater.* (2020)
3. C. Huang, Y. Ye, L. Zhao, Y. Li, J. Gu, J. *Inorg. Organomet. Polym. Mater.* **29**, 1476 (2019)
4. Y.-N. Wang, H.-X. Li, L. Jia, S.-S. Zhang, Y.-R. Zhao, L. Du, Q.-H. Zhao, *Inorg. Chem. Commun.* **110** (2019)
5. S. Chen, Z. Shi, L. Qin, H. Jia, H. Zheng, *Cryst. Growth Des.* **17**, 67 (2016)
6. X. Zhang, C. Ge, N. Zhang, Y. Duan, Y. Wang, L. Zhao, X. Zhuang, J. Li, J. Wu, Q. Yang, *Inorg. Chim. Acta* **496** (2019)
7. S.-L. Yang, Y.-Y. Yuan, P.-P. Sun, T. Lin, C.-X. Zhang, Q.-L. Wang, *New J. Chem.* **42**, 20137 (2018)
8. Y.-J. Yang, D. Liu, Y.-H. Li, G.-Y. Dong, *Polyhedron* **159**, 32 (2019)
9. K. R. Reddy, M. S. Jyothi, A. V. Raghu, V. Sadhu, S. Naveen, T. M. Aminabhavi, in *Nanophotocatalysis and Environmental Applications: Detoxification and Disinfection*, ed. By A. M. Asiri, and E. Lichtfouse (Springer Cham, 2020) p. 139
10. M. S. Jyothi, V. Nayak, K. R. Reddy, S. Naveen, A. V. Raghu, in *Nanophotocatalysis and Environmental Applications: Materials and Technology*, ed. By G. Sharma, A. Kumar, E. Lichtfouse, and A. M. Asiri (Springer, Cham, 2019) p. 83
11. R. Shwetharani, H. R. Chandan, M. Sakar, G. R. Balakrishna, K. R. Reddy, A. V. Raghu, *Int. J. Hydrog. Energy* **45**, 18289 (2020)
12. M. S. Jyothi, K. R. Reddy, K. Soontarapa, S. Naveen, A. V. Raghu, R. V. Kulkarni, D. P. Suhas, N. P. Shetti, M. N. Nadagouda, T. M. Aminabhavi, *J. Environ. Manage.* **242**, 415 (2019)
13. M. Ashafaq, M. Khalid, M. Raizada, M. S. Ahmad, M. S. Khan, M. Shahid, M. Ahmad, *J. Inorg. Organomet. Polym. Mater.* **30**, 4496 (2020)
14. S. A. A. Razavi and A. Morsali, *Coord. Chem. Rev.* **415** (2020)
15. F. Guo, Q. Yang, X. Li, *J. Inorg. Organomet. Polym. Mater.* **29**, 159 (2018)
16. D. Ma, C. Chen, M. Chen, S. Zhu, Y. Wu, Z. Li, Y. Li, L. Zhou, *J. Inorg. Organomet. Polym. Mater.* **29**, 1829 (2018)
17. F. Wang, C. Dong, C. Wang, Z. Yu, S. Guo, Z. Wang, Y. Zhao, G. Li, *New J. Chem.* **39**, 4437 (2015)
18. F. Haque, A. Halder, S. Ghosh, A. Maiti, D. Ghoshal, *Cryst. Growth Des.* **19**, 5152 (2019)
19. G. Lee, J. H. Yoon, K. Kwon, H. Han, J. H. Song, K. S. Lim, W. R. Lee, *Inorg. Chim. Acta* **513** (2020)
20. C.-L. Zhang, Z.-T. Liu, H. Xu, H.-G. Zheng, J. Ma, J. Zhao, *Dalton Trans.* **48**, 2285 (2019)
21. H.-y. Sun, Z.-r. Wang, X. Li, S. Han, J.-j. Wang, W.-f. Li, C.-l. Liu, C.-b. Li, *Inorg. Chim. Acta* **486**, 750 (2019)
22. Y.-Q. Su, Y.-H. Qu, L. Fu, G.-H. Cui, *Inorg. Chem. Commun.* **118** (2020)
23. G. Yan, G. Zhou, X. Yu, X. Jiang, H. Xia, *J. Mol. Struct.* **1074**, 393 (2014)
24. G. Liu, Y. Li, Z. Lu, X. Li, X. Wang, X. Wang, X. Chen, *CrystEngComm* **21**, 5344 (2019)

25. X.-S. Wu, J. Liang, X.-L. Hu, X.-L. Wang, B.-Q. Song, Y.-Q. Jiao, Z.-M. Su, *Cryst. Growth Des.* **15**, 4311 (2015)
26. H.-J. Zhang, P. Wang, R.-Q. Fan, Y.-W. Dong, X.-M. Wang, Y. Song, Y.-L. Wang, Y.-L. Yang, *J. Coord. Chem.* **69**, 1014 (2016)
27. Y. Wang, Y. Zhao, H. Yu, Z.-Q. Liu, L.-J. Wang, R.-Y. Huang, W. Xu, J.-F. Wu, *J. Coord. Chem.* **288** (2020)
28. A. Halder, B. Bhattacharya, F. Haque, D. Ghoshal, *Cryst. Growth Des.* **17**, 6613 (2017)
29. J. Zhou, L. Du, Y.-F. Qiao, Y. Hu, B. Li, L. Li, X.-Y. Wang, J. Yang, M.-J. Xie, Q.-H. Zhao, *Cryst. Growth Des.* **14**, 1175 (2014)
30. Z. Zhang, H. X. Sun, L. Du, M. J. Xie, J. Zhou, Q. H. Zhao, *Z. Anorg. Allg. Chem.* (2020)
31. D. M. Ciurtin, Y.-B. Dong, M. D. Smith, T. Barclay, H. C. Loye, *Inorg. Chem.* **40**, 2825 (2001)
32. M. Keikha, M. Pourayoubi, A. van der Lee, *J. Chem. Crystallogr.* **50**, 88 (2019)
33. V. A. Blatov, A. P. Shevchenko, D. M. Proserpio, *Cryst. Growth Des.* **14**, 3576 (2014)
34. Sheldrick G. M., SADAB, Program for Empirical Absorption Correction for Area Detector Data, University of Göttingen, Göttingen, 1996
35. G. M. Sheldrick, *Acta Crystallogr. Sect. C-Struct. Chem.* **71**, 3 (2015)
36. B. Pramodh, P. Naresh, S. Naveen, N. K. Lokanath, S. Ganguly, J. Panda, S. Murugesan, A. V. Raghu, I. Warad, *Chem. Data Collect.* (2020)
37. S. B. Benaka Prasad, S. Naveen, C. S. Ananda Kumar, N. K. Lokanath, A. V. Raghu, I. Daraghmeh, K. R. Reddy, I. Warad, *J. Mol. Struct.* **1167**, 215 (2018)
38. S. B. Benaka Prasad, C. S. Anandakumar, A. V. Raghu, K. Raghava Reddy, M. V. Deepa Urs, S. Naveen, *Chem. Data Collect.* **15-16**, 1 (2018)
39. 39. -N. Zhao, S.-R. Zhang, W. Wang, Y.-H. Xu, G.-B. Che, *New J. Chem.* **42**, 14648 (2018)
40. M. Yu, Y. Zhang, Y.-Q. Pan, L. Wang, *Inorg. Chim. Acta* **509** (2020)
41. S.-L. Cai, L. Lu, W.-P. Wu, J. Wang, Y.-C. Sun, A.-Q. Ma, A. Singh, A. Kumar, *Inorg. Chim. Acta* **484**, 291 (2019)
42. Z. Wei, Z.-H. Zhang, M.-M. Wang, L. Xu, B. Liu, H. Jiao, *CrystEngComm* **19**, 5402 (2017)
43. W. Xie, C. Yao, K.-Z. Shao, Y.-H. Xu, Z.-M. Su, *New J. Chem.* **42**, 20056 (2018)
44. N. Xu, Q. Zhang, B. Hou, Q. Cheng, G. Zhang, *Inorg. Chem.* **57**, 13330 (2018)
45. L. Liu, Y. Wang, R. Lin, Z. Yao, Q. Lin, L. Wang, Z. Zhang, S. Xiang, *Dalton Trans.* **47**, 16190 (2018)

Figures

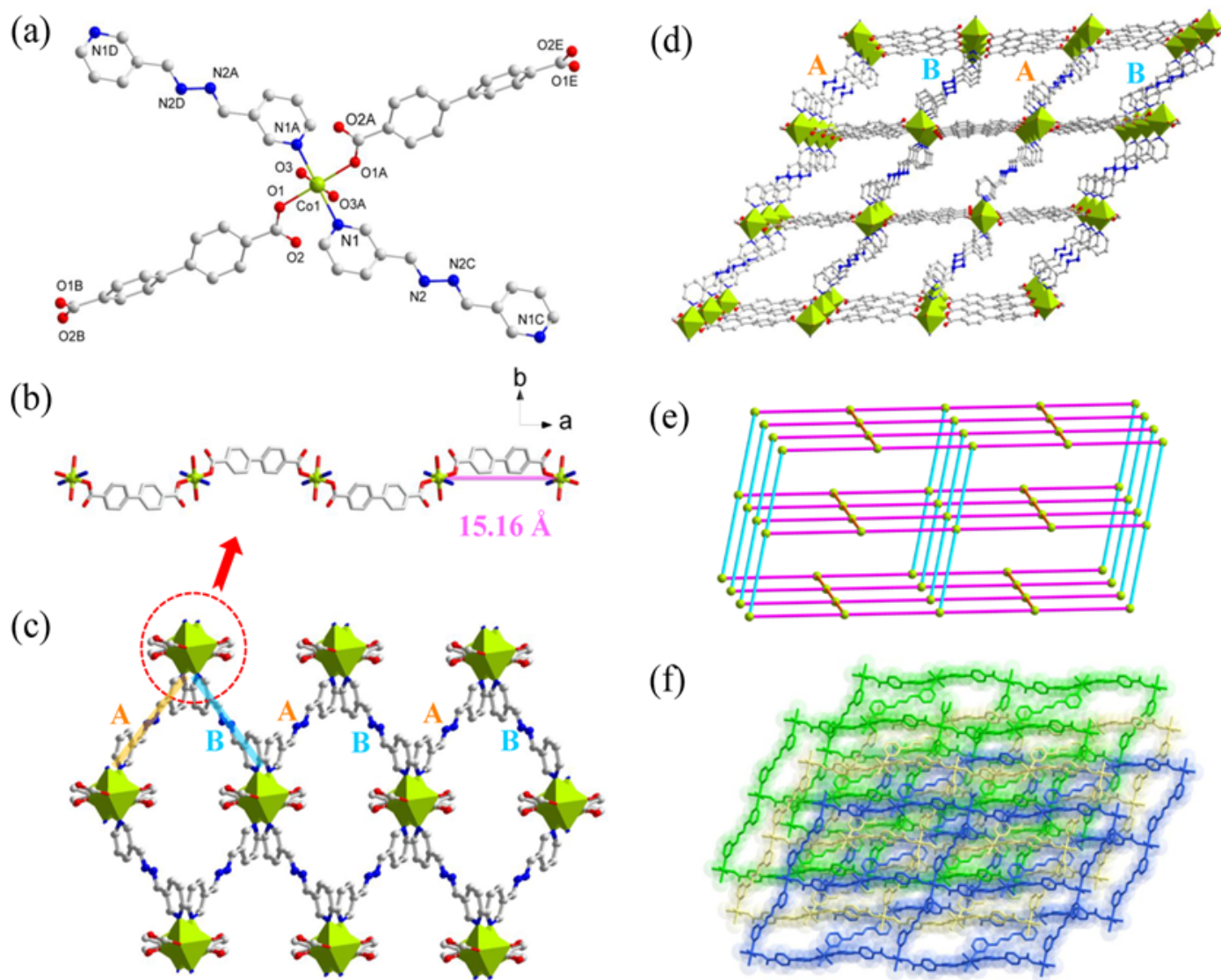


Figure 1

(a) Coordination environment of Co(II) ion in 1. All hydrogens are omitted for clarity (symmetry codes: (A) $-x + 1/2, -y + 1/2, -z$; (B) $-x, y, -z + 1/2$; (C) $-x + 1, -y + 1, -z + 1$; (D) $x - 1/2, y - 1/2, z - 1$; (E) $x + 1/2, -y + 1/2, z - 1/2$). (b) 1D linear chain generated by BPDC2- linked Co(II) centers. (c) 3-bpdb ligands linked linear chain in two directions to form 3D architecture. (d) 3D architecture of 1. (e) Topological representation of one single cds network. (f) Packing of the structure of 1 with 3-fold interpenetration

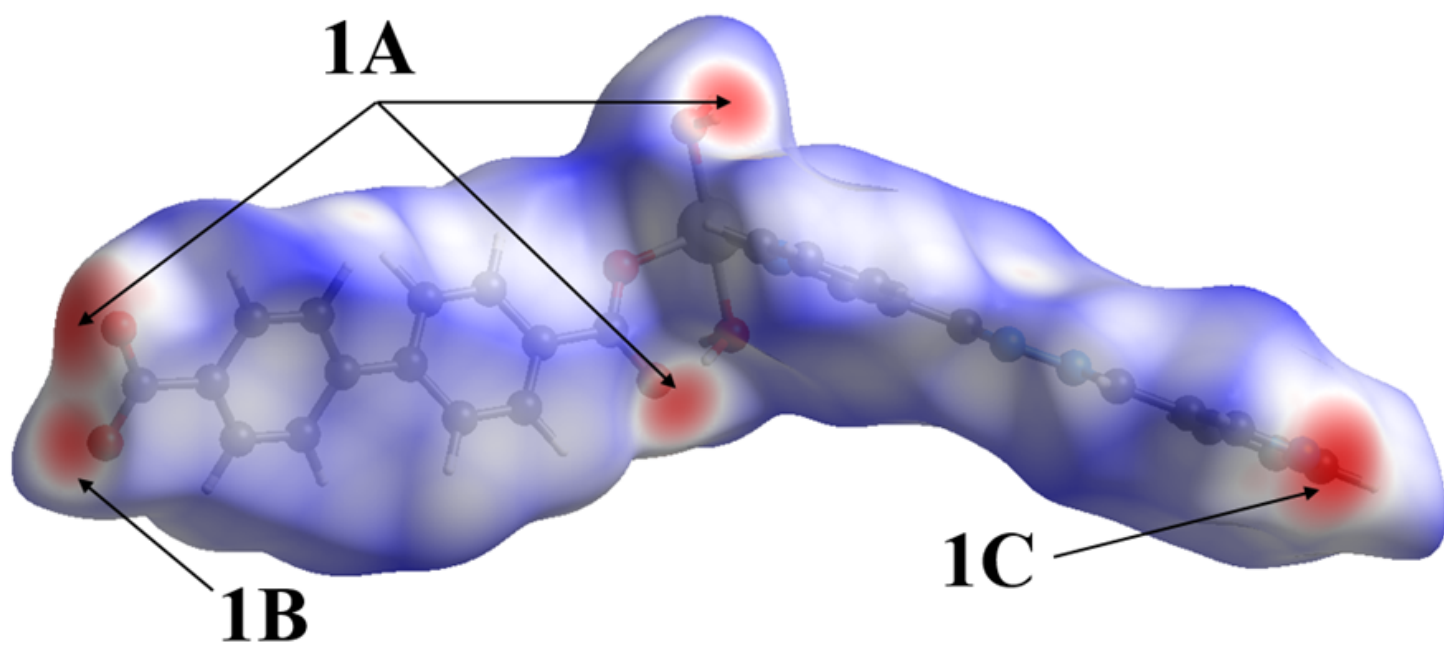


Figure 2

Hirshfeld surface mapped with dnorm of compound 1

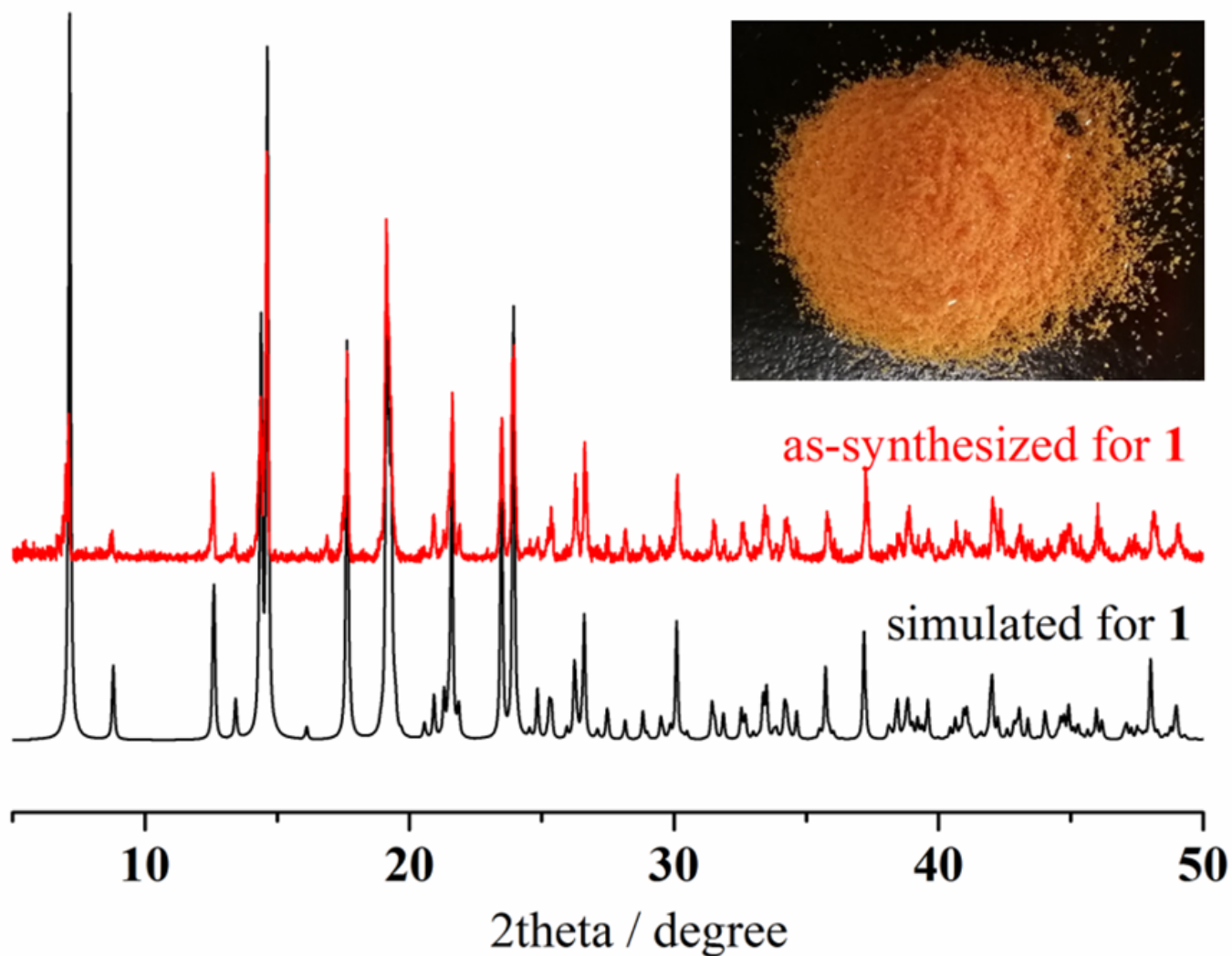


Figure 3

PXRD pattern of **1**

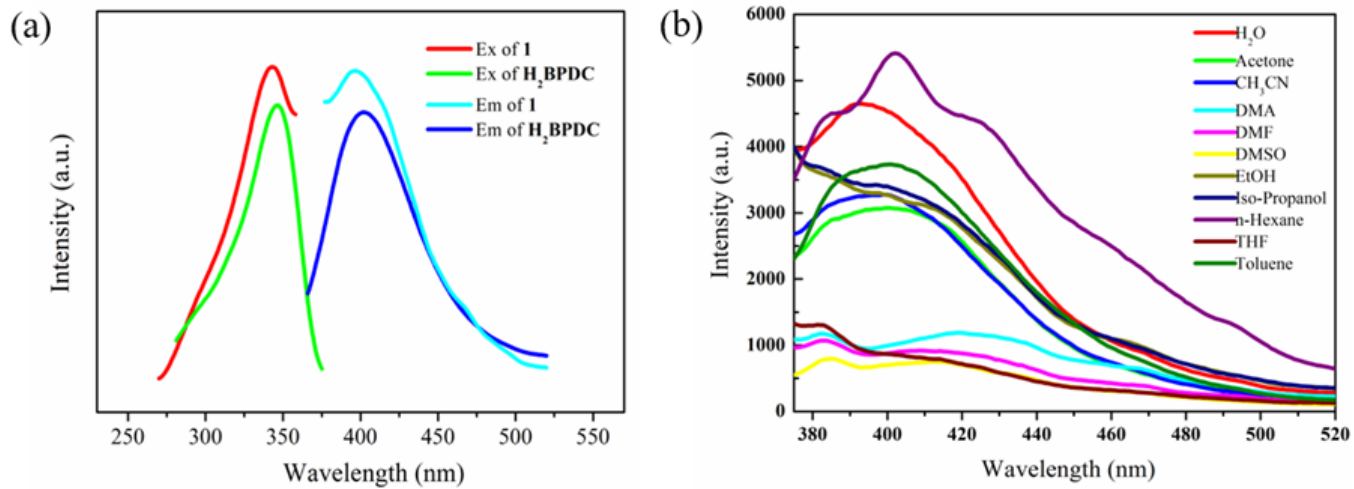


Figure 4

(a) The fluorescence spectra of **1** and the H2BPDC ligand in solid state at room temperature. (b) Luminescence emission spectra of **1** in different solutions

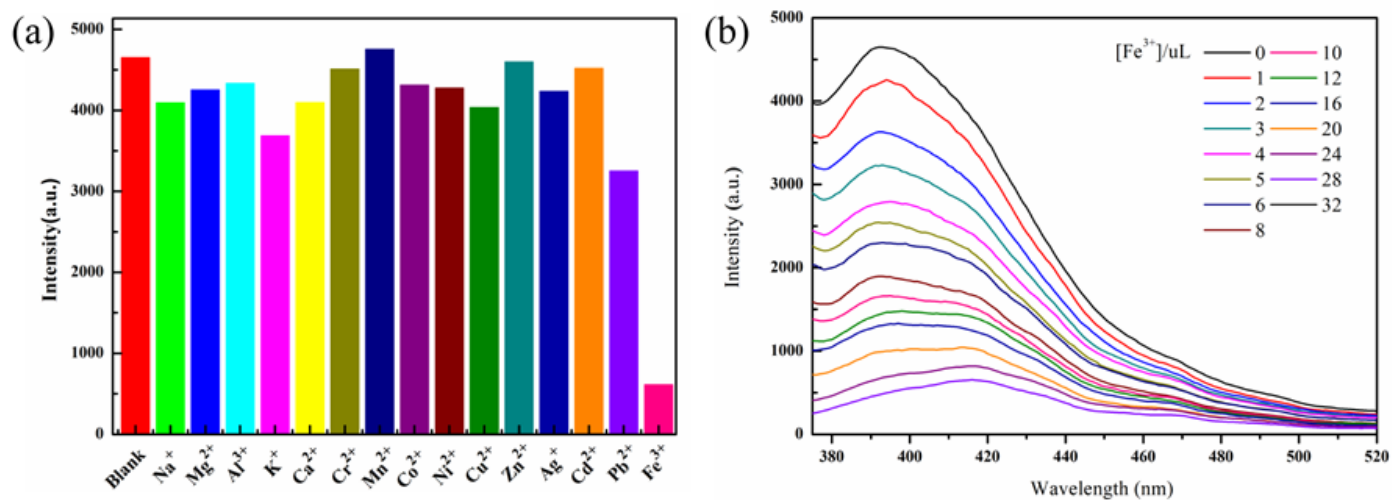


Figure 5

(a) The luminescence intensities at 393 nm of complex **1** which were dispersed in aqueous solution of different metal ions. (b) Effect on the emission spectra of **1** dispersed in aqueous solution upon incremental addition Fe³⁺ ion

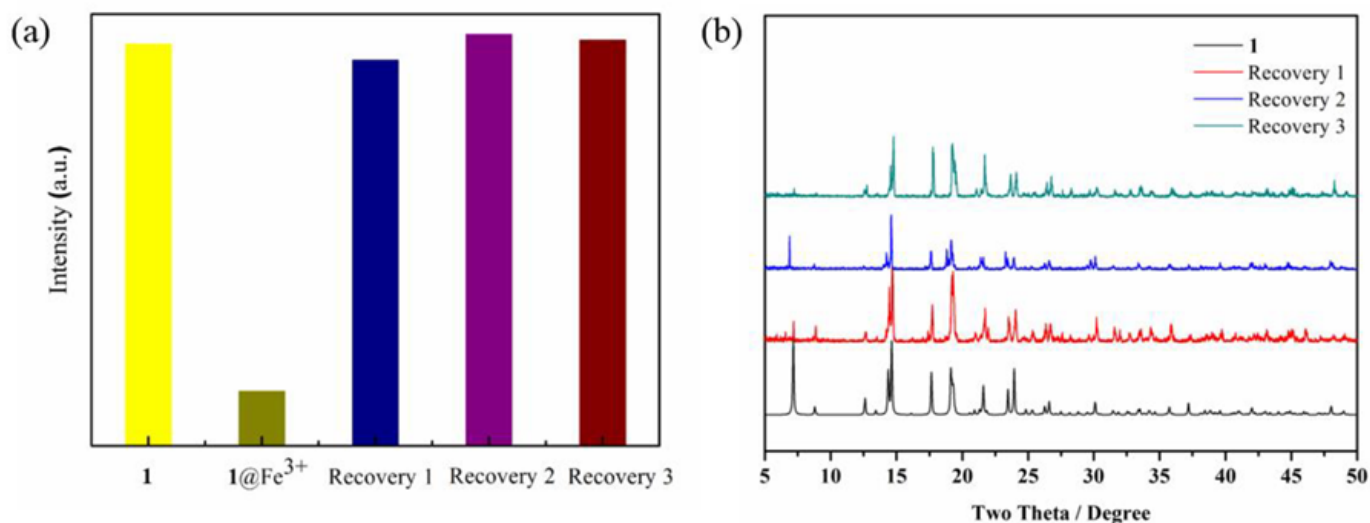


Figure 6

(a) The luminescence intensity of **1** and that found after three recycles. (b) The powder X-ray diffraction patterns of **1** after cyclic sensing Fe³⁺ ions

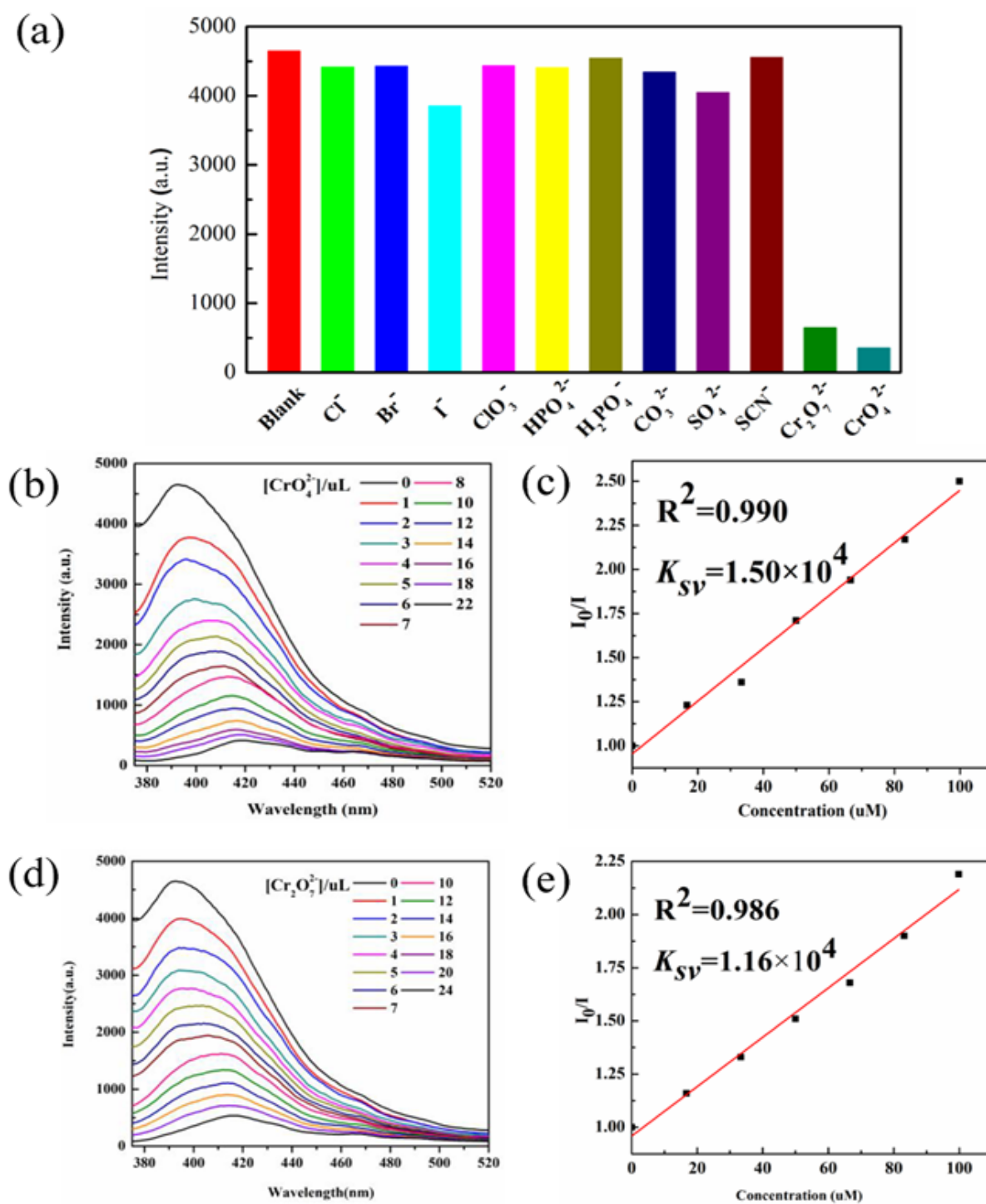


Figure 7

(a) Emission spectra of 1 dispersed in different anions solvents when excited at 346 nm. Emission spectrum of 1 upon incremental addition of (b) CrO₄²⁻ and (d) Cr₂O₇²⁻ in aqueous solution. The SV plot of I₀/I versus (c) CrO₄²⁻ and (e) Cr₂O₇²⁻ ions solution (50mM) in water

Supplementary Files

This is a list of supplementary files associated with this preprint. Click to download.

- [checkcif.pdf](#)
- [GraphicalAbstract.tif](#)
- [RevisedSupportinginformation.doc](#)